Available online at www.sciencedirect.com

ScienceDirect

Procedia IUTAM 26 (2018) 204–213

Procedia IUTAM

www.elsevier.com/locate/procedia

IUTAM Symposium Wind Waves, 4–8 September 2017, London, UK

General Sea State and Drag Coefficient Observed near Shore in Taiwan Strait

Yuan-Shiang Tsai[a]*, Wang-Ting Chang[b], Chao-Ming Yu[b], Wen-Chang Yang[b]

[a]*National centre for Research On Earthquake Engineering, NARLabs, National centre for Research On Earthquake Engineering, NARLabs 200 Sec. 3, Sinhai Road, Taipei 10668, Taiwan*

[b]*Taiwan Ocean Research Institute, NARLabs, 96 Henan 2nd Road, 80143 Kaohsiung, Taiwan*

Abstract

The general characteristics of wind waves and drag coefficient are studied using the data from the buoy observation near shore in Taiwan Strait. An algorithm of the bulk aerodynamic method using 10-minute mean wind speed and the temperature difference between the air and sea surface was developed to calculate the equivalent wind speed at 10 m in height and the surface friction velocity. The observation shows that the sea states contains a wide range of wave ages driven by the synoptic wind systems, i.e. the strong northeast monsoon in winter and southwest monsoon in summer, mixed with the thermally diurnal variation across the sea-land boundaries. The large-scale winds generate a number of swells with long fetch and the mesoscale circulation perpendicular to the main streams causing wind and wave misalignments. The drag coefficients display considerable scattering around the linear growth formulation along with the increase of neutral wind speed. This is attributed to the dependence of surface roughness on wave ages. The present observation confirms that the drag coefficients are sensitive to the sea state described using the Charnock constant and hence the wave ages.

Peer-review under responsibility of the scientific committee of the IUTAM Symposium Wind Waves.

Keywords: Drag coefficient; surface roughness, diurnal cycle, buoy observation

1. Introduction

The interaction between the atmosphere and ocean is the physical process responsible for the transfer of momentum flux across the air-sea interface. From the microscale turbulent exchange to the macro scale ocean circulation and the global climate change, the surface wind stress τ is the most significant driving force to produce momentum transfer on the sea surface and lead to wave growth. For field experiments with measurement of mean quantities, the bulk aerodynamic scheme [1] is developed to parameterize the sea surface fluxes in which the wind stress is connected to the wind speed at 10 m in height via a drag coefficient with the relation:

Peer-review under responsibility of the scientific committee of the IUTAM Symposium Wind Waves.
10.1016/j.piutam.2018.03.020

$$\tau = \rho_a C_D U_{10}^2 \tag{1}$$

where ρ_a denotes the air density, U_{10} denotes the wind speed at the height of 10 m, and C_D denotes the drag coefficient. The surface wind speed profile in adiabatic condition is modelled in the logarithmic formulation:

$$\mathrm{u(z)} = \frac{u_*}{k}\ln\left(\frac{z}{z_o}\right) \tag{2}$$

where $u_*=(\tau/\rho_a)^{1/2}$ represents the friction velocity, k represents Karman constant, z represents the vertical height, and z_o represents the surface roughness length. In combination of equation (1) and (2) the drag coefficient is therefore expressed as follows:

$$C_{DN} = \left(\frac{u_*}{U_{10N}}\right)^2 = \left(\frac{k}{ln(z_{10}/z_o)}\right)^2 \tag{3}$$

where z_{10} represents 10 m in height and the subscription N represents under the atmospheric neutral stability. Comprehensive studies in terms of drag coefficient have been particularly carried out under the circumstance of neutral stratification. Earlier studies prior to 1975 suggested that the sea surface drag coefficient is constant [2]. Subsequent experiments over the past decades remarked that the drag coefficient increased with the increase of the neural wind speed [2, 3, 4, 5, 6]. A linear relation is formulated with:

$$C_{DN} = (a + bU_{10N}) \times 10^{-3} \tag{4}$$

where a and b are constant coefficient determined from the field or laboratory data. However, the increase of the drag coefficient is not valid in high wind speeds in excess of 40 m/s observed under the action of hurricanes [7].

Equation (3) indicates that the drag coefficient is also the surface roughness dependent. In the circumstance beyond the aerodynamic smooth surface, with the increase of wind speed, small scale wind waves grow and generate a rougher surface to effectively attract the momentum from the airflow. Charnock (1955) proposed that the surface roughness is proportional to the wind stress known as the Charnock relationship

$$z_o = C_h \frac{u_*^2}{g} \tag{5}$$

where C_h denoted the Charnock parameter, and g denoted gravitational acceleration. Charnock parameter was originally given to be a constant value. Using C_h=0.014, equations (2), (3), and (5) are solved under a specific wind speed to give the coefficients in drag coefficient equation (4) for a=0.75 and b=0.067 [3, 8].

However, the values of C_h vary in different observation results ranging from 0.011 to 0.018, which implies that for a given wind speed the surface roughness may be different. The reason is due to that in a practical field the development of wind waves and hence constitution of sea states relate to not only wind speed but other important factors, for example, the limitation of fetch and duration, wind and wave directional misalignment, and coastal shoaling. A sea state is characterised using the waves age C_p/u_* or C_p/U_{10} where C_p represents the phase velocity at the spectral peak of waves. Hence, the surface roughness is suggested to wave age dependent and the Charnock parameter is described using a power law formulation [11]:

$$z_o \frac{g}{u_*^2} = A\left(\frac{C_p}{u_*}\right)^{-B} \tag{6}$$

where A and B represents the constant coefficients. Guan and Xie [4] derived the linear growth of the drag coefficient along with the increase of the wind speed. Their analysis resulted the dependence of drag coefficient on Charnock parameter with a=0.78 and b=0.475$C_h^{1/2}$. The young wind waves with smaller Charnock constant causing larger wind shear than mature waves are explained from the FETCH experiment of Drennan et al. [12].

In the present study, wind and waves were observed using a buoy in Taiwan Strait offshore Changhua Taiwan. The place is well known for strong winds particularly in the winter season. The original objective of this program was to assess the site for establishment of an offshore wind farm. For the geographic position of the Strait, the wind

waves are primarily generated by the seasonal monsoons mixed with the secondary effect of thermal circulation across the sea-land boundaries. This phenomenon have not been fully examined to characterise the local sea states in terms of general sea states and the dependence of drag coefficient on wave ages. The results of the surface parameterizations are used for the engineering practice for wind turbine design. More importantly, the local drag coefficient parameters can improve the prediction accuracy of ocean and wave models, which are very useful for future wind farm operations with regard to wind and wave simulation. Currently the models only employ the drag coefficients interpreted from the 10 m mean wind speed.

2. Site description and buoy system

The wind and waves were observed using a wave following discus buoy with the size of 2.5 m in diameter developed by the Coastal Ocean Monitoring Centre. One year measurement was conducted during the period of August 2012 to July 2013 in Taiwan Strait, 14 km from the coast of Fangyuan Township (120°12′0″, 23°59′54″), Changhua County, in the middle west of Taiwan where the water depth was approximately 40 m. The site was 50 km north of the Tropic of Cancer. Strong solar heating induced diurnal circulation at the sea-land boundaries particularly in summer. Figure 1 shows the location of the experimental site and the buoy system. The Strait exposes to open water facing East China Sea in the northeast direction and South China Sea in the southwest direction, respectively. Hence, swells generated by large-scale trade winds propagating to the site were recorded.

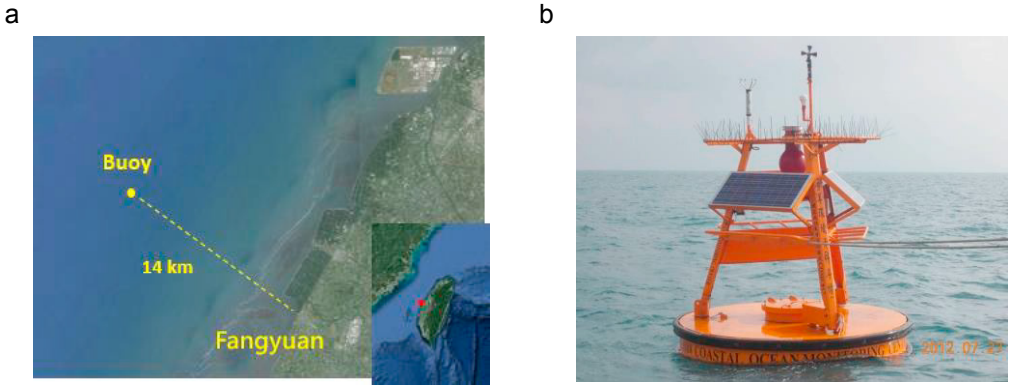

Fig. 1. The observation site and buoy deployed offshore of Fangyuan Township; (a) geographic position of the observation site near shore with a large scale map in right bottom; (b) the buoy system and instrumentations.

The instruments included the sensors to measure the wind speed, air and sea surface temperature, pressure and buoy motions. The wind speed and direction were observed using a two-dimensional ultrasonic anemometer, Gill-1390, and propeller anemometer, Young-05106 at the height of 2.9 m and 3.2 m, respectively. The buoy motions represented by linear accelerations and rotation angles in the three directions were measured using Watson SHR-A 1360-2A-30/105. The component of vertical accelerations was computed to obtain sea surface elevations. Besides, subsurface currents were observed using the ADCP, SonTek ADP0.5. Three solar panels with 80 W in total were employed for the power supply. The data logger simultaneously recorded the wind speed, air and sea temperature, pressure, and buoy motions for the first 10-minute in every hour with a sampling rate of 2 Hz. Mean values of the 10-minute data were transferred to office via wireless communication. Due to the weak sunlight in winter the system was automatically reduced the recording frequency to every four hours in December 2012. However, the sunlight was further weak in January 2013 to cause the power supply complete failure. Besides, the mooring anchored disconnected under the strong wave force in April 2013. The buoy recorded the passage of typhoon Soulik in 13 July 2013 with the wind speed in excess of 20 m/s. However, the typhoon event is excluded in the present study. 7673 10-minute datasets in 10 month observation are available in which the neutrally stratified condition over the sea are studied.

3. Data analysis

3.1. Buoy motion correction

The buoy title and rotation following the sea surface distort measurement results of the instantaneous wind velocity and wave heights. The apparent wind velocities are corrected using the method developed by Edson et al. [13] for which a coordinate transformation matrix was employed to correct the surface motions and obtain true wind velocities. The transform method was also applied for the measured vertical accelerations. The wave elevations are directly calculated from the integration of corrected accelerations. The integration induced a low frequency noise, which was removed using a high-pass filter Hp described as follows:

$$\eta(t) = Hp\left(\iint(\ddot{z}(t)dt)dt\right) \tag{7}$$

where η denoted the surface wave elevation and $\ddot{z}$ denoted the vertical acceleration after the motion correction. The significant wave height was calculated using the zero-up crossing method. The wave direction was assessed from the co-spectrum and quadrature spectrum direction, which was directly given by the buoy measurement system.

3.2. Atmospheric stability

To evaluate the atmospheric stability for the identity of neural wind, the 10-minute mean wind speed and temperature in air and sea were used to compute the bulk Richardson number Ri_b, introduced by Hsu [14] expressed as the following form:

$$Ri_b = \frac{gz_{10}(T_a - T_s)}{(T_a + 273)U_{10}^2} \tag{8}$$

where T_a represented the air temperature and T_s represented the sea temperature, respectively. The dimensionless stability parameter, z/L, where L denotes the Monin-Obukov length, is assessed from Richardson number giving by

$$\begin{cases} z/L = 7.6Ri_b, & T_a < T_s \\ z/L = 6.0Ri_b, & T_a > T_s \end{cases} \tag{9}$$

for unstable and stable condition. The neutral stratification is indicated in the range of $-0.1<z/L<0.1$ [9].

3.3. Surface roughness

For a sea state mixed with wind waves and swells, Taylor and Yelland [15] suggested that wave slopes were appropriate to describe sea surface roughness scaled by the significant wave height with the dimensionless relation:

$$\frac{z_o}{H_s} = 1200\left(\frac{H_s}{L_p}\right)^{4.5} \tag{10}$$

where H_s represented the significant wave height and L_p represented the peak wavelength. The peak wavelength is calculated from the dispersion relationship using wave peak period T_p at the peak frequency of the wave spectrum. Hence, the phase speed of the dominant waves at the spectral peak is $C_p=L_p/T_p$. Because the present observation shows a certain number of swells mixed with young wind waves equation (10) is used to estimate the sea roughness.

3.4. Calculation for U_{10} and u_*

The power law is employed to convert the wind speed at the measurement height at 2.9 m to the equivalent wind speed at 10 m in height described as follows:

$$\frac{U(z_{10})}{U(z_{2.9})} = \left(\frac{z_{10}}{z_{2.9}}\right)^{\alpha} \tag{11}$$

where $U(z_{2.9})$ denotes the reference wind speed at the measurement height 2.9 m and α denotes the power exponent. The surface friction velocity was evaluated using the velocity profile of Monin-Obukhov similarity theory (MOST)

$$u_* = k\mathrm{u(z)}\left(\ln\left(\frac{z}{z_o}\right) - \Psi_m\left(\frac{z}{L}\right)\right)^{-1} \tag{12}$$

where z_o was evaluated from equation (10) and Ψ_m denotes the stability function with the formulation given by [14]

$$\Psi_m(z/L) = \begin{cases} -5z/L, & z/L < 0 \\ 1.0496(-z/L)^{0.4591}, & z/L > 0 \end{cases} \tag{13}$$

Assuming that the vertical wind profile formulated using the power law is equivalent to the diabetic surface boundary layer described by MOST, at the height of 10 m the power exponent can be approximated by

$$\alpha \approx 0.1\phi_m \tag{14}$$

where $\phi_m(z/L)=kz/u_*\partial u/\partial z$ represents the dimensionless wind shear expressed by the following relation:

$$\phi_m(z/L) = \begin{cases} 1 + bz/L, & z/L < 0 \\ (1 - az/L)^P, & z/L > 0 \end{cases} \tag{15}$$

where a=15, b=4.7, and p=-1/4 in the flat and homogeneous terrain [16].

A C++ code was written to compute U_{10} and u_*. Over a general sea surface, Hsu et al. [14] recommended that the power exponent was 0.11, which was used to be an initial value. The power exponent and hence the friction velocity were iteratively solved after the convergence of the power exponent with $|\alpha_1-\alpha_o|<10^{-3}$ where α_1 was the solution of the next iteration of α_o.

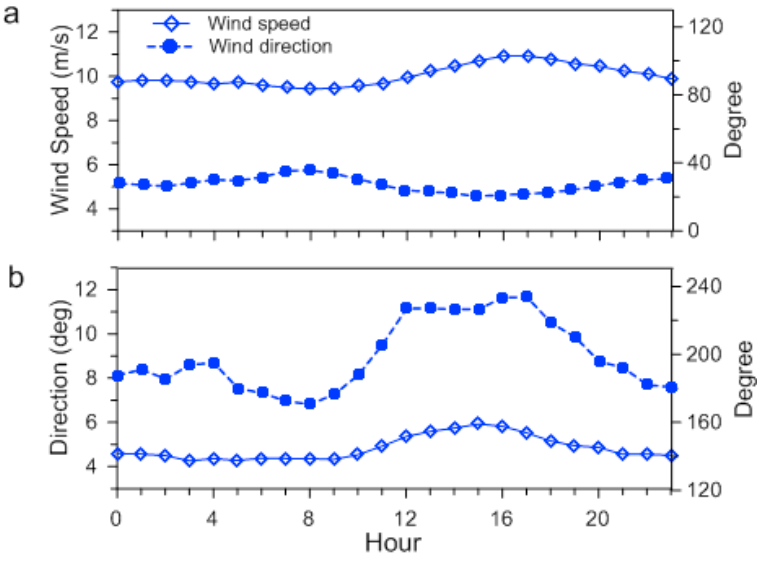

Fig. 2. Influence of thermal circulation on the synoptic winds causing the diurnally periodic motion for wind speed and direction, (a) northeast wind, (b) southwest wind.

4. Results and discussions

4.1. General features of wind and waves

The buoy observation shows that the wind in the Taiwan Strait is driven by two major synoptic frontal systems. The long period from late September to March of the next year is predominated by northeast monsoon which carries strong and cold wind with the maximum wind speed in excess of 20 m/s. In contrast, during the period from May to

August the warm air of southwest wind becomes dominant with the moderate wind speed not exceeding 10 m/s. As shown in figure 1(a) of the right bottom, the winds for these two prevailing directions travel long distance from open waters into the Strait. The generated swells are frequently observed at the observation site.

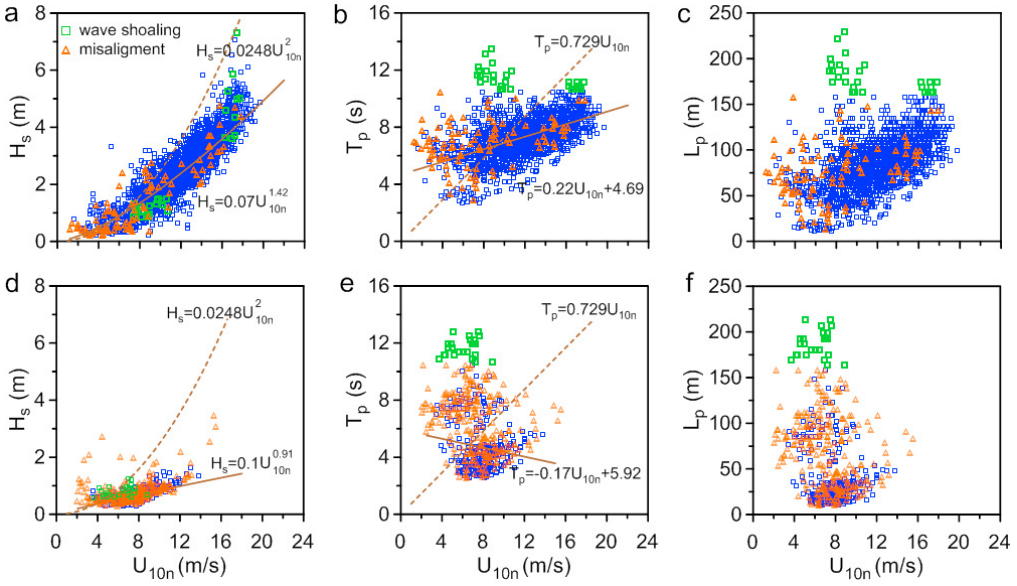

Fig. 3. Observation of wind wave data plotted against 10 m neutral wind speed, U_{10n} for northeast wind (upper row) and southwest wind (lower row), wave shoaling for $L_p/h>4$, misalignment of wind and wave for $|\Delta\theta|>30^o$, solid line: the present curve fitting; dash line, JONSWAP results [6]: (a) significant wave height; (b) wave period at the spectral peak of waves; (c) wavelength at the spectral peak of waves.

Apart from the synoptic weather systems, the thermally stratified mesoscale circulation across sea-land boundaries contributes the secondary effect on the wind patterns. The onshore wind in day and offshore wind in night is approximately perpendicular to the frontal wind. The mixed wind of the two scales is illustrated in figure 2. The daily ensemble average in the wind speed and direction clearly show the diurnal cycle. With the relatively strong wind from the northeast monsoon, the mean wind speed is approximately 10 m/s, however, varying with the amplitude of 1.5 m/s as displayed in figure 2(a). The thermally stratified flow increases the wind speed in day with the maximum wind speed appearing at 16:00 in the afternoon. The wind direction slightly varies within 15^o in one day. This steady wind direction indicates that the sea surface is acted on by the cold wind with a long fetch and duration. In contrast, with the relatively weak wind dominated from the southwest airflow, the mean amplitude increases to 1.7 m/s. The diurnal variation is significant observed for the wind direction with the directional change more than 60^o as shown in figure 2(b). The wind direction is altered by the sea breeze forming the west-southwest wind in day and land breeze forming the south-southeast wind in night. In this aspect of the directional change, the misalignment between wind and waves is substantial and the sea state is usually limited by a short fetch and duration. It is observed that in the absence of the synoptic winds, the mesoscale circulation becomes predominant in the coastal and near shore region. This slight wind speed is generally less than 6 m/s under the stratification condition leading to very young sea state.

Because the mesoscale diurnal cycle substantially influences the wind direction, particularly for the southwest wind, the general sea states are exhibited according to the two synoptic winds. The mean wind directions are limited to $0^o<\theta<45^o$ for northeast wind and $190^o<\theta<235^o$ for the southwest wind. In fact, these two ranges of direction are generally parallel to the coast. The waves travelling in these two directions could have been experienced a long distance movement from the East China Sea or South China Sea, respectively. Figure 3 demonstrates the development of the significant wave height, peak wave period, and peak wavelength depending on the neutral wind speed, U_{10n}. Considering the wave shoaling with $L_p/h>4$ where h denotes the water depth and the substantial misalignment between wind and wave defined with $|\Delta\theta|>30^o$ where $\Delta\theta$ denotes the directional difference between

the wind and waves, the data are distinguished in three groups. As shown in figure 3(a), the significant wave height increases with the increase of the wind speed. For the northeast wind with steady wind direction and stronger wind speed, the surface waves generated are considerably higher than those generated by southwest wind. However, using JONSWAP observation, Cater [16] derived that the relation between H_s and the wind speed is H_s=0.0248U_{10n}^2 which gave significantly larger H_s in the fully developed sea state when compared with the present observations with H_s=0.07$U_{10n}^{1.42}$ for the northeast wind and H_s=0.1$U_{10n}^{0.91}$ for the southwest wind.

The relationship between the peak wave period and neutral wind speed are depicted in figure 3(b). Regarding the surface waves generated by the northeast monsoons, the development of peak wave periods is considerably different from the JONSWAP fetch limit results with linear growth formulation T_p=0.729U_{10n} [16]. The present growth rate of the peak periods is lower, showing short wave periods with U_{10n}<10 m/s, however, longer wave periods in the strong wind speed with U_{10n}>10 m/s. It is likely that the winter sea state contains a certain number of swells which reduces the growth of peak wave periods in terms of the wind speed. For the wind from southwest, the data show distinct three groups with the peak wave periods approximately 2<T_p<6 s for pure wind waves, 6<T_p<10 s for swells, and T_p>10 s for the shoaling waves. The evolution of peak wavelengths calculated from the dispersion relationship using T_p along with the wind speed is given in figure 3(c). The patterns distributed are in analogous to T_p showing three different characterises of waves.

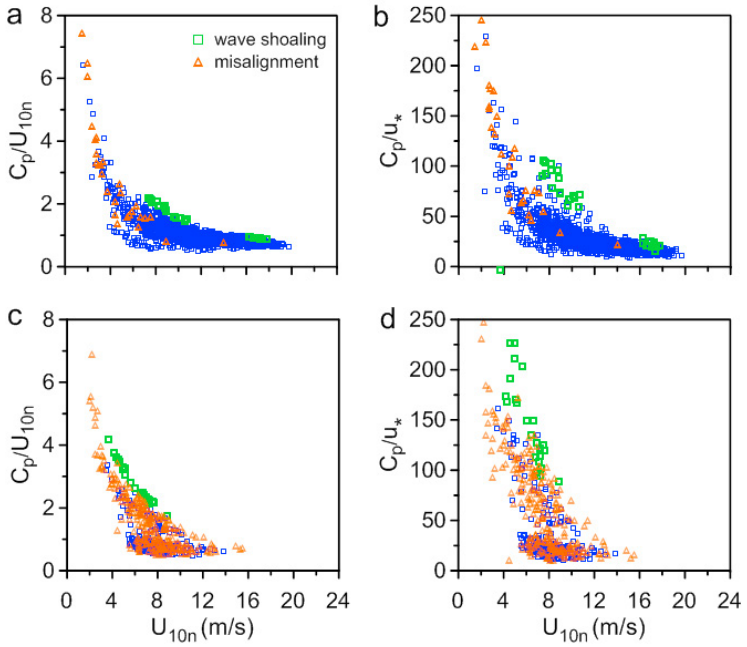

Fig.4. Relation between the wave age and the neutral wind speed at 10 m in height for northeast wind and southwest wind: (a) and (b) wave age represented by C_p/U_{10n} and C_p/u_* for northeast wind, (c) and (d) wave age represented by C_p/U_{10n} and C_p/u_* for southwest wind.

Figure 4 discusses sea state patterns generated by the two large-scale wind systems with northeast wind in figure 4(a) and 4(b) and southwest wind in figure 4(c) and 4(d). A criterion with C_p/U_{10n}=1.2 is used to characterize the wind sea and swell condition. When C_p/U_{10n}<1.2 the state are young and formed with short and steeper wind waves. In contrast, when C_p/U_{10n} >1.2, the sea waves is mature or fully-developed and dominated by long swells [12]. As displayed in figure 4, the wave age decreases with the increase of the wind speed. This implies that under the strong wind action the generated young waves can effectively attract energy from the wind until the waves become fully-developed. Under the northeast wind brought by the cold fronts with the period of several days, the sea states are formed with the mixed young and mature waves. The shoaling waves spreads in the upper bond of the distribution of wave ages. In addition, the wind and wave misalignment is observed in the weak wind speed with large wave ages observed in the termination of the cold front with the wind direction changed from northeast to south wind.

The wind sea, swell and shoaling phenomena are clearly appeared for the southwest wind in figure 4(c) and 4(d) with three individual groups represented by the upper shoaling waves, middle misalignment and mature waves, and lower young waves. The explanation is that the relatively weak wind from southwest in summer is considerably affected by the diurnally thermal stratified flow which is nearly perpendicular to the main stream direction. Hence, the composed wind direction is spatially varied when the wind moves along the near shore area. This results a large amount of wind and wave misalignments because the wave direction cannot immediately response to the change of the wind direction. The directional change also leads to a short duration of wind action and produces the young sea state as shown in figure 4(c) and 4(d) in the lowest groups. Nevertheless, the wind waves generated in a far distance away may still grow to mature waves as given in the middle groups in figure 4(c) and 4(d). Interestingly, the wave age patterns show a gap between the middle and lowest groups just with C_p/U_{10}=1.2 in figure 4(b) at the wave age criteria to classify young and mature waves. Observed from figure 4(d), the gap is located at C_p/u_*≈30-40. The value is close to the HEXOS results showing C_p/u_*≈37-36 with C_p/U_{10}=1.2 [17].

4.2. Roughness length and drag coefficient

In examination of the surface roughness depending on wave ages, the misalignment data shown in figure 4 are not considered because it is difficult to account the wind shear direction along with the wave direction. Also the shoaling waves are not included. The sea state subjects to the two synoptic winds collapse together in the roughness dimensionless form. Figure 5(a) shows the relationship between dimensionless roughness and wave age in comparison with the result of Drennan and Graber [12], who studied the sea surface roughness for developing wind waves with the wave age C_p/u_*<20 formulated with the relationship:

$$\frac{z_o}{\sigma} = C\left(\frac{C_p}{u_*}\right)^{-D} \tag{16}$$

where the coefficient C=13.4 and D=3.4 and σ represents the root mean square of the sea surface elevation. The present result gives C=146 and D=4 for the mixed sea state with a wide range of wave age 8<C_p/u_*<250, C=51 and D=3.66 for the developing sea state with C_p/u_*<30, and C=1380 and D=4.55 for the old sea state with C_p/u_*>30. The multiplicative factor is significant larger and the power exponent is smaller than that of Grennan and Graber [12]. This indicates that the roughness at the observation site is higher in the young waves, however, decaying more quickly to the state of lower roughness in the mature sea. The Charnock parameter depends on the wave age is displayed in figure 5(b). The best regression fitting line makes A=60 and B=2.67 in equation (6), for which the consequence is analogous to the case using the dimensionless parameter σ with a larger multiplier and smaller power exponent when comparing with previous studies with C ranging from 0.8 to 1.89 and D ranging from 1 to 1.7.

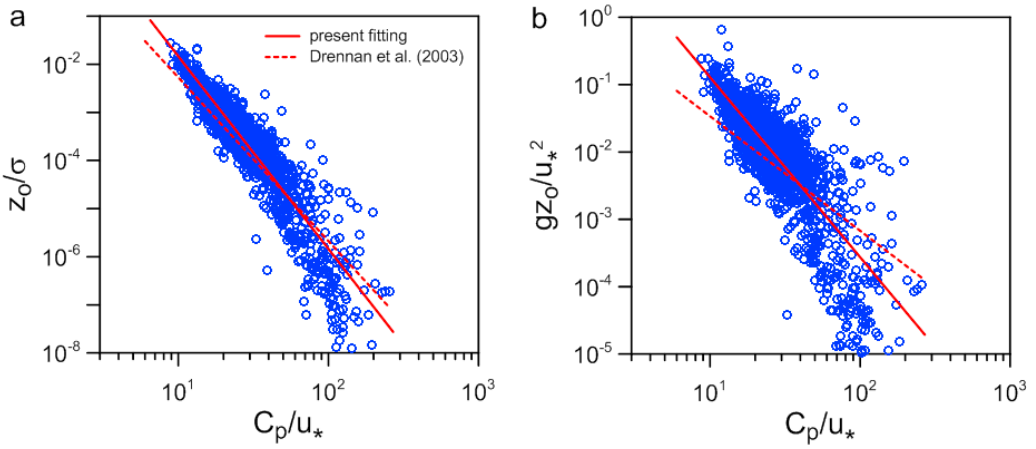

Fig.5. Dimensionless roughness length versus wave age in the mixed sea state without consideration of wave misalignment and shoaling: (a) non-dimensionalized using root mean square of sea surface elevation; (b) shown by Charnock constant.

The observation of the neural drag coefficient C_{DN} related to the wind speed at 10 in height is demonstrated in figure 6(a) in comparison with the previous results of drag coefficient curves. The linear regression fitted to the present data gives the following result:

$$C_{DN} = (0.13 + 0.124U_{10N}) \times 10^{-3} \tag{17}$$

with a=0.13 and b=0.124 which is close to the result of Drennan et al. [18] with a=0.15 and b=0.117. Yelland and Taylor [19] revealed that the drag coefficient increase with the decrease of the wind speed when U_{10N}<6 m/s. However, this phenomenon is unlikely to be observed in the present results.

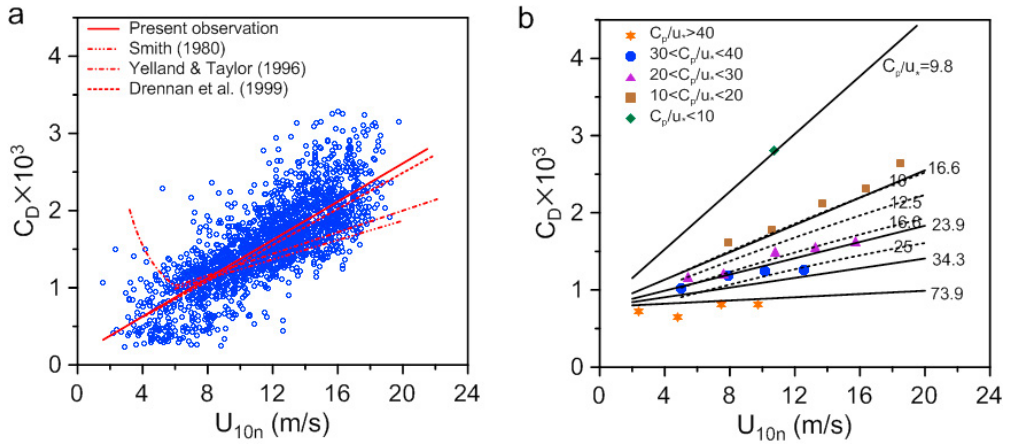

Fig.6. Drag coefficients in terms of the wind speed in the neutral stratification (a) total data points without wave misalignment and shoaling comparing with previous results (b) classified by the five groups of wave ages, solid line: the present curve fitting; dash line, FETCH results [12].

Substantial scattering of the data points is displayed in figure 6(a). This is likely due to the sea state containing a wide range of wave ages. It has been noted that wave ages determine the degree of wave development for which the momentum flux generated over a young wind sea larger than mature sea [12, 17]. The observed drag coefficients were re-examined by distinguishing the wave ages to five groups with C_p/u_*<10, 20>C_p/u_*>10, 30>C_p/u_*>20, 40>C_p/u_*>30, and C_p/u_*>40. In each group, C_{DN} was averaged for 2 m/s bins of the wind speed. Figure 6(b) shows the development of C_{DN} with respect to U_{10N} for each group of the wave age. Significant difference of the drag coefficients between the young and old sea state is observed. This is attributed to the developing wind waves with large steepness, that is, the wave slopes, which increase the transfer of the momentum flux between the air-sea interfaces [20]. Using the formulation of Guan and Xie [4] with a=0.78 and b=0.475$C_h^{1/2}$, the linear five growths subjected to mean wave ages are shown in figure 6(b) with the solid lines and the numeric values of mean wave ages at the right-hand side. The results confirm that the drag coefficient is wave age dependent. The FETCH wind sea data giving the drag coefficient curve in terms of wind speed and wave age [12] are plotted using the dash line in figure 6(b). For the old waves with C_p/u_*=25 the agreement with the present result is reasonably good. However, the discrepancy increases with the decrease of the wave age. For example, with very young wave age C_p/u_*=10, the difference to the FETCH results becomes significant. The growth process of very young waves requires further research.

5. Conclusion

The buoy observation shows the complex sea states generated by two seasonal monsoons with the prevail wind directions form the northeast and southwest in different seasons affected by the thermal circulation across the sea-land boundary. The diurnal cycle wind considerably rotates the direction of the relatively weak southeast airflow, contributing a large number of wind-wave misalignments. In addition, swells are usually observed at the

experimental site because the two large-scale winds with the directions from the open oceans. Hence, the sea state in Taiwan Strait contains a wide range of wave ages from very young waves to mature waves. The study shows that the dimensionless roughness lengths are wave age dependent for which the roughness is larger than previous experiments in the young developing waves. The roughness length rapidly decays with the increase of wave ages in the swell conditions. In spite of the mixed sea state, the mean drag coefficients show a slightly larger growth rate than previous studies with the increase of the mean wind speed in the neutral stratification. However, the scattering of individual dataset reveals that the drag coefficient is influenced by wave ages. The wind stress coefficient significantly increases in the young sea states when compared with those in the mature sea. A linear growth of the drag coefficient to the neutral wind speed depending on the Charnock parameter is in good agreement with the theoretical formulation.

Acknowledgements

The authors wish to express their acknowledgement to National Science Council for the project funding (NSC 99-3113-P-492-002). We are indebted to Coast Ocean Monitoring Centre, National Cheng Kung University for the deployment and maintenance of the buoy.

References

1. C. W. Fairall, J. B. Edson, S. E. Larsen, and P. G. Mesteyer, Inertial-dissipation of air–sea flux measurements: a prototype system using real-time spectral computations, *Journal of Atmospheric and Oceanic Technology*, 1990; **7**: 425-453.
2. S. D. Smith, Wind stress and heat flux over the ocean in gale force winds, *Journal of Physical Oceanography*, 1980; **8**, 709-726.
3. J. R. Garratt, Review of drag coefficients over oceans and continents, *Monthly Weather Review*, 1977; **105**, 915-929.
4. J. Wu, Wind-stress coefficients over sea surface near neutral conditions-A revisit, *Journal of Physical Oceanography*, 1980; **10**, 727-740.
5. W. G. Large and S. Pond, Open ocean momentum flux measurements in moderate to strong winds, *Journal of Physical Oceanography*, 1981; **11**, 324-336.
6. C. Guan, and L. Xie, On the Linear Parameterization of Drag Coefficient over Sea Surface, *Journal of Physical Oceanography*, 2004; **34**, 2847-2851.
7. M. D. Powell, P. J. Vickery, and T. A. Reinhold, Reduced drag coefficient for high wind speeds in tropical cyclones, *Nature,* 2003; **422**, 279-283.
8. V. K. Makin, V. N. Kudryavtsev, C. Mastenbroek, Drag of the sea surface, 1995; *Boundary-Layer Meteorology*, 1995, **73**, 159-182.
9. G. L. Geernaert, K. B. Katsaros, and K. Richter, Variation of the drag coefficient and its dependence on sea state, *Journal of Geophysical Research*, 1986; **91**, 7667-7679.
10. W. Lin, L. P. Sanford, and S. E. Suttles, Drag coefficient with fetch-limited wind waves, *Journal of Physical Oceanography*, 2002; **32**, 186-209.
11. S. D. Smith, R. J. Anderson, W. A. Oost, C. K. Maat, J. Decosmo, K. B. Katsaros, K. L. Davidson, K. Bumke, L. Hasse, and H. Chadwick, Sea surface wind stress and drag coefficients: the HEXOS results, *Boundary-Layer Meteorology*, 1992; 60, 109-142
12. W. M. Drennan and H. C. Graber, On the wave age dependence of wind stress over pure wind seas, 2003; *Journal of Geophysical Research*, **108**, FET 10-1-10-12.
13. J. B. Edson, A. A. Hinton, K. E. Prada, J. E. Hare, and C. W. Fairall, Direct covariance flux estimates from mobile platforms at sea, *Journal of Atmospheric and Oceanic Technology*, 1998; **15**, 547-561.
14. S. A. Hsu, Estimating overwater friction velocity and exponent of power-Law wind profile from gust factor during storms, *Journal of Waterway, Port, Coastal, and Ocean Engineering*, 2003; **129**, 174-177.
15. P. K. Taylor, and M. Y. Yelland, The dependence of sea surface roughness on the height and steepness of the waves, *Journal of Physical Oceanography*, 2001; **31**, 572-590.
16. D. T. J. Cater, Prediction of wave height and period for a constant wind velocity using JONSWAP formulae, *Ocean Engineering*, 1982; **9**, 17-33.
17. S. D. Smith, R. J. Anderson, W A. Oost, C. K. Nico Matt, J. DeCosmo, K. B. Katsaros, K. L. Davidson, K. Bumke, L. Hasse, and H. M. Chadwick, Sea surface wind stress and drag coefficients: The HEXOS results, *Boundary-layer meteorology*, 1992; **60**, 109-142.
18. W. M. Drennan, K. K. Kahma, K. K., and M. A. Donelan, On momentum flux and velocity spectra over waves, *Boundary layer Meteorology*, 1999; **92**, 489–515.
19. M. Yelland and P. K. Taylor, Wind stress measurements from the open ocean, *Journal of Physical Oceanography*, 1996; **25**, 541-558.
20. J. W. Miles, Generation of surface waves by wind, *Applied Mechanics Reviews*, 1997; **50**, R5-R9.